



OPEN

Strontium isotope proxy of sedimentological records reveals uplift and erosion in the Southeastern Neo-Tethys ocean during the late Cretaceous

Amin Navidtalab^{1✉}, Hamzeh Mehrabi², Hadi Shafaii Moghadam^{1,3} & Hossain Rahimpour-Bonab²

The mutual interplays between plate tectonic processes, orogenesis and continental uplift, high-flux magmatism, and high sedimentation rates can affect the geochemical signatures and composition of marine sediments. Here, we examine two major disconformities, the Cenomanian–Turonian boundary (CT-ES) and the middle Turonian (mT-ES) exposure surfaces, from the Upper Cretaceous sedimentary successions of the southeastern Neo-Tethys Ocean in the Zagros Basin (Iran). The disconformities are expressed as distinct positive peaks in rubidium (Rb) contents and $^{87}\text{Sr}/^{86}\text{Sr}$ isotopic ratios of carbonates. The $^{87}\text{Sr}/^{86}\text{Sr}$ values of samples bracketing the disconformities in seven well cores give average age ranges of 94.4–93.6 Ma for the CT-ES and 91–86 Ma for the mT-ES. These ages fall in the timespan of forearc/ophiolite formation through subduction initiation in the Neo-Tethys realm (southern margin of Eurasia), high convergence velocities between Arabia and Eurasia, and blueschist exhumation. All these processes involved buckling of the Neo-Tethyan lithosphere, initiating the Neo-Tethys closure and a high erosion rate on the Eurasian margin. The first two mechanisms exerted considerable compressional forces on the adjacent carbonate platforms, reactivated basement faults, and led to the uplift and erosion of the Arabian Plate, which provided the high contents of Rb and the high $^{87}\text{Sr}/^{86}\text{Sr}$ ratios in the carbonates.

The Cretaceous period coincided with significant global changes, including sea-level oscillations, biota speciation, and extinction, intense climate variations, large igneous province (LIPs) magmatism, vigorous tectonic activity, and major changes in continental configuration, and resultant oceanic anoxic events (“*deoxygenation*”)^{1–4}. Understanding the timing and tempos of these events—and thus their causes—needs detailed studies on the Cretaceous marine sedimentary rocks, which is the main aim of this paper. The causes of these events can be controlled by either far-field, worldwide, or local tectonic events.

The Late Cretaceous epoch was characterized by an acceleration in plate movements, extensive formation of oceanic crust in the Neo-Tethys Ocean (Fig. 1A), and uplift in the nearby continents along the southern parts of the Mediterranean region, including Cyprus, Turkey, as well as in Caucasus, Iran (Zagros; Fig. 1B) and Oman (i.e., *Bitlis-Zagros suture zone*)^{5–11}. The subduction initiation during the middle Cretaceous along the Eurasian (Iranian) margin led to ophiolite formation and extension in the overlying continental crust, which resulted in a remarkable structural reconfiguration of the Zagros area, including the reactivation of basement faults and halokinetic movements^{12–17}. The obduction of the Zagros–Oman ophiolites led to further changes in plate kinematics and the closure of oceanic basins in Oman (*Arabian Plate*)¹⁸. The obduction also changed the rate of subduction of the Neo-Tethyan oceanic lithosphere beneath Eurasia (including Iran and Anatolia, e.g., Agard et al.¹⁹) and triggered the uplift of the overlying continental crust, leading to enhanced subduction erosion in Zagros⁷. However, there are no detailed studies on the consequence of this continental uplift and the sea-level changes during the Late Cretaceous.

¹School of Earth Sciences, Damghan University, Damghan 36716-45667, Iran. ²School of Geology, College of Science, University of Tehran, Tehran, Iran. ³Department of Geological Engineering, Karadeniz Technical University, 61100 Trabzon, Turkey. ✉email: a.navidtalab@du.ac.ir

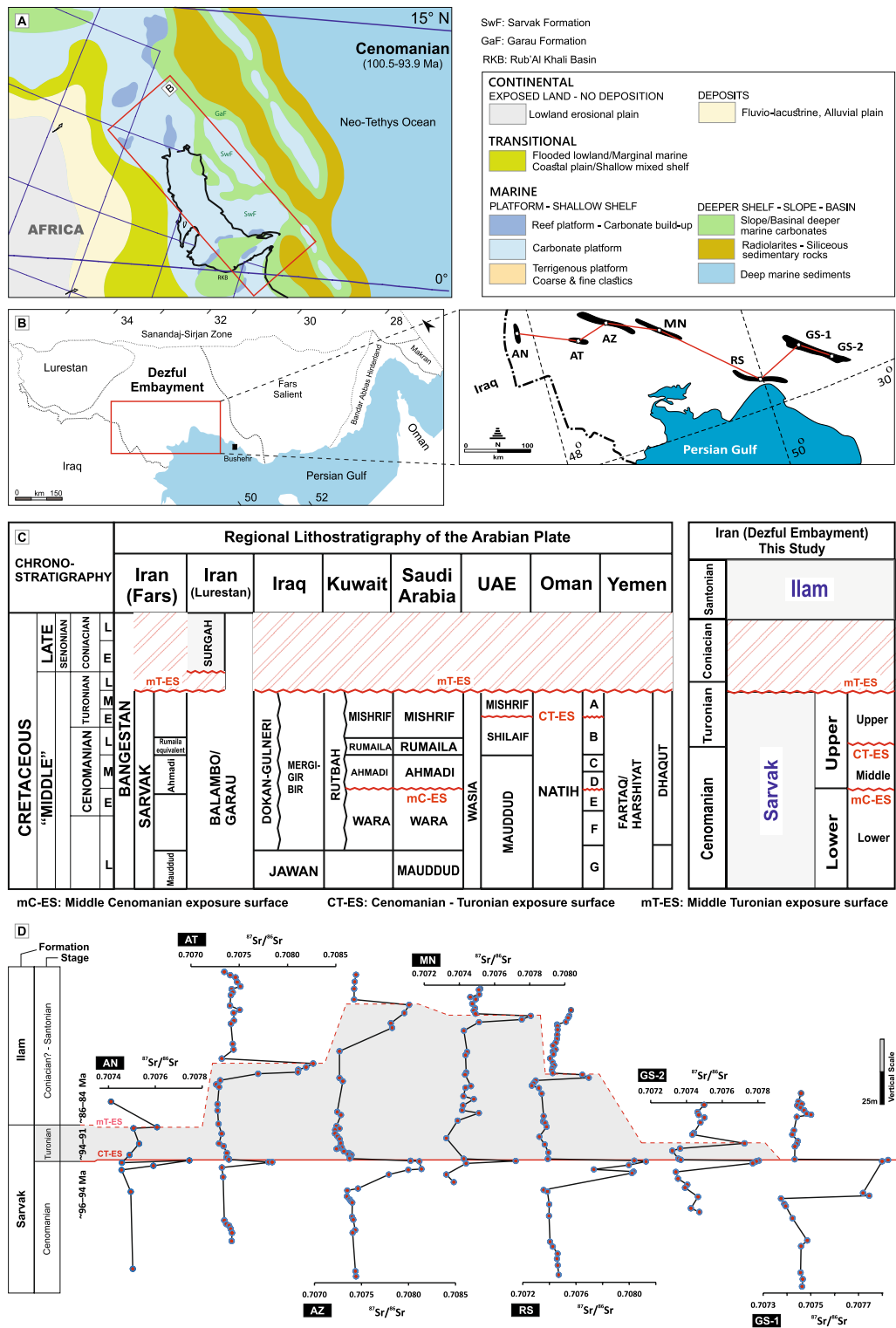


Figure 1. (A) Paleogeographic reconstructed map of the southeastern margin of the Neo-Tethys Ocean during the Cenomanian³⁶; (B) the extension of the Zagros geological subdivisions including the study area (Dezful Embayment); (C) Stratigraphic column of the upper Cretaceous rocks in the Middle East and the Dezful Embayment of Zagros Basin in Iran (adopted with some modifications from⁷⁵). (D) Rb-uncorrected ⁸⁷Sr/⁸⁶Sr values recorded for well cores along a W-E trend in Zagros showing two positive peaks (except for GS-1 with merged disconformities) associated with the CT-ES and mT-ES disconformities. Cores AZ, MN, and GS-2 are from this study. Core RS is from²², cores AN and AT are from²⁰, and Core GS-1 is from²¹.

Consequently, several paleo-highs (i.e., *horsts and salt domes*) formed along the Zagros Basin (Fig. 1A–B), where shallow marine carbonate platforms were exposed and eroded^{9,20–23}. These exposure events are expressed as three regional disconformities within the Cenomanian–Turonian sequences throughout the Middle East, including the west, south, and southwest of Iran^{23–25}, Oman^{26,27}, UAE^{28,29}, Qatar³⁰, Iraq^{31,32}, and Turkey³³. These disconformities represent; (a) the mid-Cenomanian exposure surface (mC-ES), which is traceable throughout the Arabian Plate, (b) the Cenomanian/Turonian boundary exposure surface (CT-ES), which is variably developed and preserved, and (c) the mid-Turonian exposure surface (mT-ES), regionally developed across the Arabian Plate (Fig. 1C).

Earlier discussions have been conducted on the disconformities in the Zagros Basin, covering sedimentological, paleontological, geochemical, and petrophysical aspects⁹. Nevertheless, comprehensive documentation regarding the causal factors, timing, and hiatus durations of these disconformities is lacking and requires further exploration. There are several speculations about the origin and causal factor(s) of these disconformities, including regional uplift (e.g. Berberian and King¹⁰), ophiolite obduction²², peripheral bulging (e.g. Hollis³⁴), block faulting and salt diapirism¹⁶, subduction initiation along the Bitlis-Zagros suture zone (e.g. Maffione et al.³⁵), and tectonic inversion⁹.

This study specifically focuses on the cores recovered from oil wells in the Dezful Embayment of the Zagros Basin. The basin was a component of the southeastern Neo-Tethyan carbonate platforms located between paleolatitudes of 0° and 15°N during the Late Cretaceous (Fig. 1A–B)³⁶. We isotopically examine the Cenomanian/Turonian (CT-ES) and mid-Turonian (mT-ES) disconformities within the upper Cenomanian–Santonian carbonate successions in a WSW–ESE trend (Fig. 1D) from the southeastern segment of the Zagros Basin of Iran (Fig. 1B). The overall aim is to identify the driving forces behind the formation of CT-ES and mT-ES disconformities documented in the Cenomanian–Santonian carbonate sequences. To accomplish this, we initially assess them through chemo-stratigraphical studies (involving Rb, Sr elemental concentration, and ⁸⁷Sr/⁸⁶Sr isotope ratios), aiming to determine the onset and duration of each associated hiatus. Subsequently, we compare all significant tectonic–magmatic events, such as ophiolite obduction, peripheral bulging, subduction initiation along the Bitlis-Zagros suture zone, and tectonic inversion, along with their respective dating, to the acquired absolute ages of the disconformities. This comparison aims to elucidate the primary causes behind these disconformities. Additionally, it allows us to deduce the driving factor behind the sea-level changes throughout the SE Neo-Tethys Ocean during the Late Cretaceous, as well as the origins of high Rb and ⁸⁷Sr/⁸⁶Sr uptakes.

Geological setting and stratigraphic background

The Zagros Basin is divided into several structural zones, including the Dezful Embayment—the targeted zone of this study—, Izeh, Lurestan, Fars, and the Persian Gulf (Fig. 1B). The Upper Cretaceous sedimentary sequences in this basin consist of neritic carbonate rocks of the Sarvak and Ilam formations (Cenomanian–Santonian), forming the second most important hydrocarbon reservoir in this region and providing the core materials for this study (Fig. 1B). The studied samples were collected from a west-to-east traverse of oilfields along the southwestern Zagros for Rb elemental content and Sr isotopes analyses (Fig. 1D).

This study includes samples from shallow-water carbonates (ramp-type platforms with predominantly neritic facies and minor pelagic facies), encompassing 361-m thick carbonates in Azadegan (AN), 245-m thick Abteymour carbonates (AT), 275-m thick Ahwaz carbonates (AZ), 145-m thick Marun carbonates (MN), 220-m thick Rag-e Sefid carbonates (RS), 157-m thick Gachsaran 1 (GS-1), and 100-m thick Gachsaran 2 (GS-2) carbonates (Fig. 1B and D). Data for the AN, AT, RS, and GS-1 well cores have been previously published^{20–22}, while data for the AZ, MN, and GS-2 cores have been analyzed during this study.

Sedimentological logs of these three new wells are presented in Fig. 2. The total studied interval consists of three third-order sequences of Cenomanian (Sv_Cen), Turonian (Sv_Tur), and Coniacian?–Santonian (Il_San) ages. Each sequence comprises open marine (middle ramp, outer ramp, and basin) facies in the TST (transgressive systems tract) and inner ramp (lagoon, shoal, and reef-talus) facies in the RST (regressive systems tract). A general ramp-like carbonate platform model was proposed for these sequences in the Dezful Embayment³³. The diagenetic history of these sequences encompasses alterations in marine (micritization, bioturbation, isopachous marine cementation; Fig. 3), two stages of meteoric (dissolution/karstification, collapse brecciation, silicification, paleosol formation, meteoric drusy and bladed calcite cementation; Fig. 3), and shallow to deep burial (mechanical to chemical compaction, blocky calcite cementation, stylolite-related dolomitization, recrystallization, pyritization, and fracturing; Fig. 3) realms²².

Geochemical logs of the studied cores are presented in Figs. 4, 5 and 6 for the AZ, GS-2, and MN wells, respectively. As shown in these logs, the CT-ES occurs on the top of inner- to proximal outer-ramp facies and is ascribed to the latest Cenomanian. The mT-ES, however, shows variable underlying facies due to irregular erosion and duration^{9,20–22}. Due to the lack of precise isotopic data, these two exposure surfaces were considered as a single disconformity in earlier studies (e.g. Hollis³⁴, Hajikazemi et al.³⁷). However, detailed geochemical-isotopic studies^{23,25,38} have revealed that these are two different exposure surfaces but were merged as a result of severe deep-reaching diagenesis and erosion in some cases. The CT-ES is characterized by younger karstification processes and a short-duration hiatus (< 1 myr) along with very negative $\delta^{13}\text{C}$ and $\delta^{18}\text{O}$ values (to -10.0‰ and -7.0‰ , respectively), high Rb contents, and high radiogenic ⁸⁷Sr/⁸⁶Sr ratios. The mT-ES has a similar expression but with mature karstification, mostly higher ⁸⁷Sr/⁸⁶Sr ratios, and quite a long (> 3 myr) hiatus^{20–23}.

Methods

Due to monotonous neritic deposits, sample collection for microfacies and geochemical analyses was in the range of ~ 3 m along the stratigraphic drilled cores. However, it decreased to ~ 0.5 m around the karstified intervals of the paleo-exposure surfaces. We have collected 524 samples for petrographic study and 100 samples for

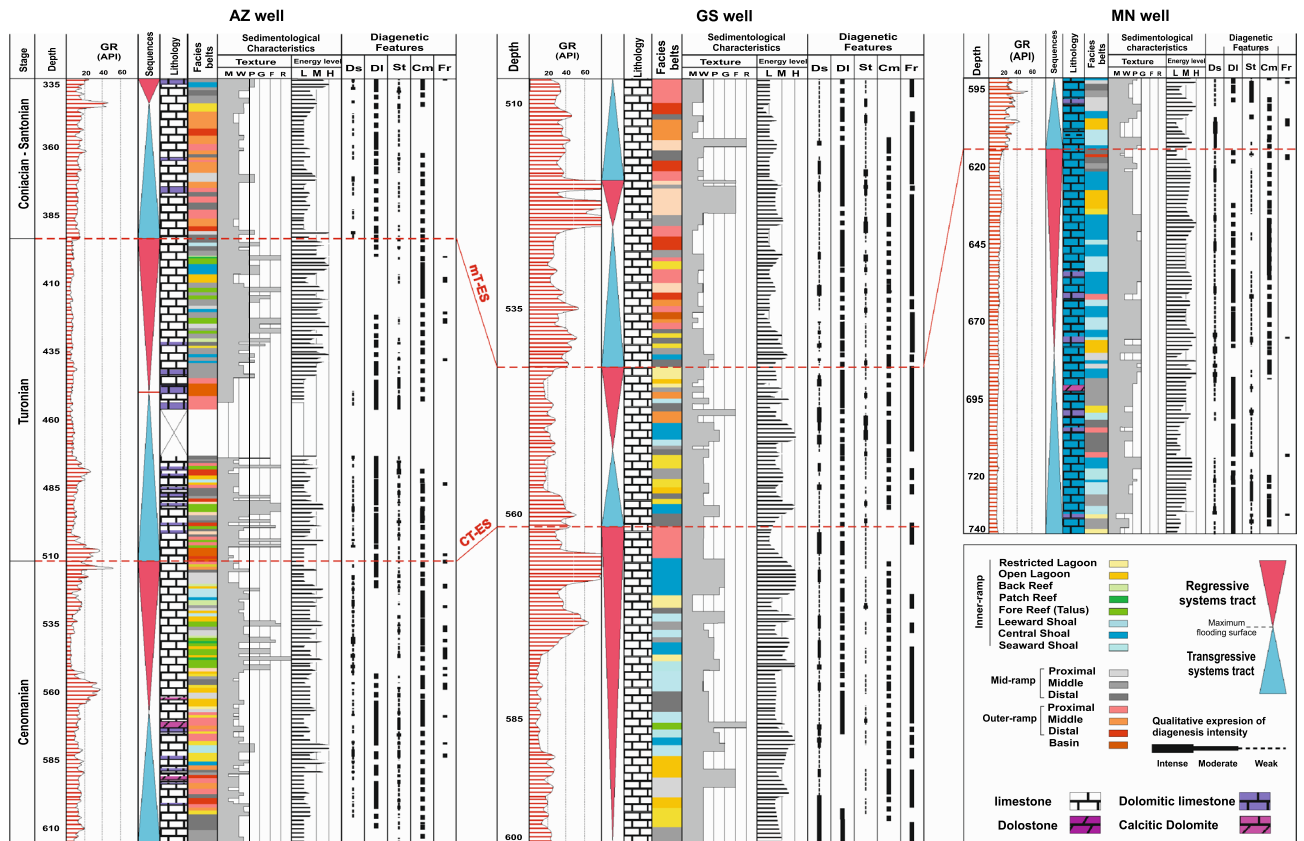


Figure 2. Sedimentological logs of the studied cores AZ, GS-2, and MN showing facies associations and depositional environment, diagenetic features, and Gamma ray (GR) logs. The mid-Turonian (mT-ES) and Cenomanian–Turonian boundary (CT-ES) disconformities are shown. Diagenetic features include Ds: dissolution; Dl: dolomitization; St: staining; Cm: cementation; Fr: fracturing.

geochemical analyses (*Sr isotopes and Rb elemental content*) from the newly studied cores (AZ, MN, and GS-2). Here, we also describe our previous Sr isotope data for some cross sections including AN, AT, RS, and GS-1.

We applied the method developed by Navidtalab et al.²² for Sr isotope stratigraphy (SIS) of disconformities in carbonates. The most fine-grained portion of carbonate samples (bulk rock) was powdered with a handheld micro-drill and measured for their $^{87}\text{Sr}/^{86}\text{Sr}$ ratios (see Table 1 in supplementary data) via Thermo Scientific TRITON thermal ionization mass spectrometer (TIMS) at the Boston TIMS Facility, USA. Rubidium (Rb) content was measured using isotope dilution (s.d. 0.3%) at Boston University, USA.

Strontium was extracted through applying standard ion-exchange methods, for loading on rhenium filaments. Isotopic fractionation was corrected through normalizing results to $^{87}\text{Sr}/^{86}\text{Sr} = 0.11940$. Any inter-laboratory bias corrections were carried out for the samples since a value of 0.7102248 ± 0.000014 (2 s.e., $n = 11$) was presented by the utilized standard SRM (NIST) 987³⁹. Constants and equations introduced by Faure and Mensing⁴⁰ were applied to correct the $^{87}\text{Sr}/^{86}\text{Sr}$ values of the analyzed samples for in-situ decay of Rb elemental content delivered by clay minerals⁴¹.

The precise stratigraphic position of disconformities and the duration of their associated hiatuses were assessed by applying the method developed by Navidtalab et al.²², through which bulk carbonates were sampled by excluding conspicuous diagenetic products including stylolites, fractures, veins, filling cements, and large bioclasts. Then, the $^{87}\text{Sr}/^{86}\text{Sr}$ log was produced for each well core. To determine the numerical age of the strata and evaluate the durations of any hiatus, the selection of the analyzed samples was performed by considering the following criteria: (a) diagenetic examinations to avoid the inclusion of diagenetically altered samples; (b) utilizing $\delta^{13}\text{C}$ values within the range of 0–6‰ and $\delta^{18}\text{O}$ within the range of –4.5–1‰, respecting the isotopic composition of early Late Cretaceous shallow water carbonates^{42–44}; (c) considering elemental contents such as $\text{Mg} < 100$ ppm, $\text{Sr} > 800$ ppm^{41,45–47}, $\text{Mn} < 225$ ppm, $\text{Fe} < 1200$ ppm, and $\text{Rb} \leq 2$ ppm, indicating less-altered samples²²; and (d) ensuring Sr/Rb ratios are ≥ 200 to indicate minimal incorporation of ^{87}Sr through ^{87}Rb decay^{22,41,48}.

Regarding the uncertainties arising from analytical error and those indicated by the Look-up Table (1 σ mean), the calculated mean numerical ages of the analyzed samples depict an uncertainty of ± 1.65 Ma. These age determinations find additional support from biostratigraphic studies, with the Geological Time Scale 2020⁴⁹ serving as the reference for defining stage boundaries. To refine the estimation of hiatal duration, consideration is given to the altered sediments situated between the reliable samples that provide numerical ages. The sedimentation rate of the limestone strata is factored in to calculate the time span of the altered carbonates. Subsequently, the

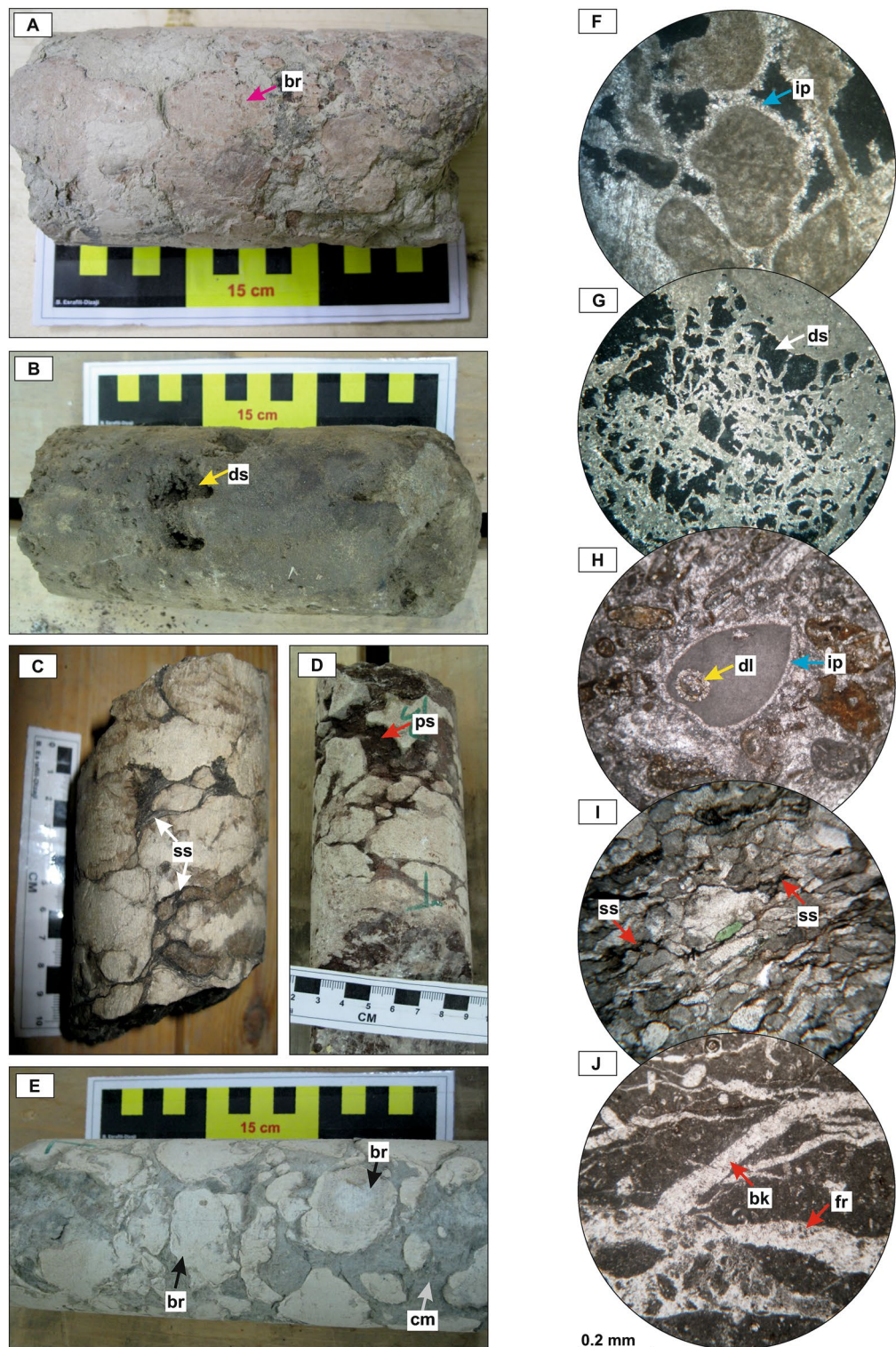


Figure 3. Core photos and photomicrographs of major diagenetic alterations of the Sarvak and Ilam formations in the studied wells. (A): brecciation (br); (B, G): dissolution (ds); (C), I: stylolite and solution seams (ss); (D): paleosol (ps); (E): brecciation (br) and clay-rich matrix (cm) between the breccias; (F): isopachous cementation (ip); (H): dolomitization (dl) and isopachous cementation (ip); (J): fracturing (fr) and blocky calcite cementation (bk). Photos F and G in XPL, H to J in PPL.

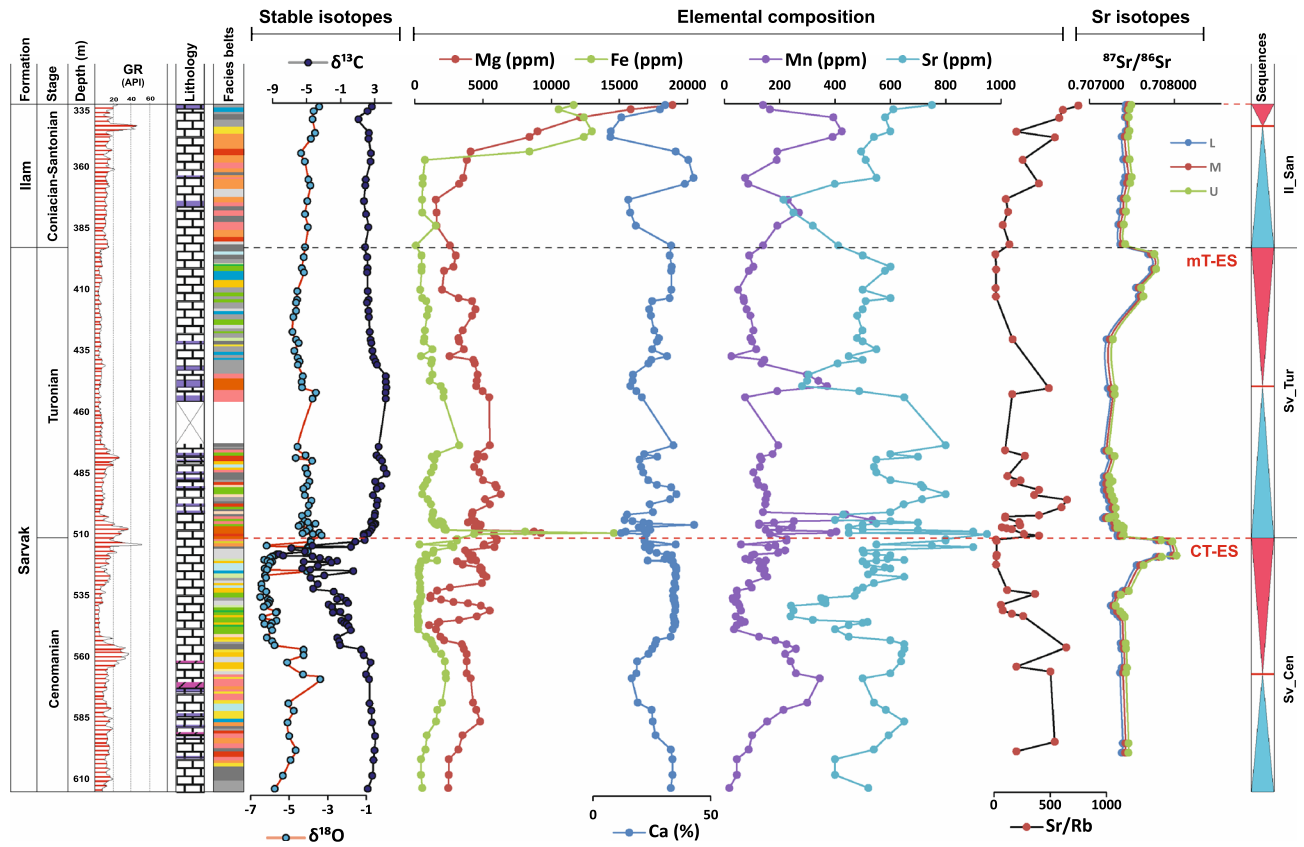


Figure 4. Carbon and oxygen stable isotopes, elemental compositions²³, Rb-corrected $^{87}\text{Sr}/^{86}\text{Sr}$ ratios, and Rb elemental data of the Sarvak and Ilam formations in well AZ. Rb elemental data are from this study. For lithology and facies pattern, please refer to Fig. 2.

calculated time derived from numerical ages is subtracted by the time span acquired from the sedimentation rate, yielding the duration of hiatus²².

Results

Core Azadegan (AN)

The $^{87}\text{Sr}/^{86}\text{Sr}$ ratios of the analyzed samples vary between $0.7074106 \pm 12 \times 10^{-6}$ to $0.7077455 \pm 20 \times 10^{-6}$, with two positive peaks at CT-ES (742–734 m) and mT-ES (691–683 m). The overall Rb concentration fluctuates from 35 to 45 ppm.

Core Abteymour (AT)

The $^{87}\text{Sr}/^{86}\text{Sr}$ ratios in core AT range from $0.707262 \pm 34 \times 10^{-6}$ to $0.708266 \pm 38 \times 10^{-6}$. The CT-ES and mT-ES in this section, are represented by two positive peaks around 298.7–291.9 m and 242.5–225 m depth, respectively. For the altered samples, the $^{87}\text{Sr}/^{86}\text{Sr}$ ratios vary between $0.707803 \pm 24 \times 10^{-6}$ and $0.707841 \pm 38 \times 10^{-6}$, just beneath the CT-ES, and range from $0.707695 \pm 24 \times 10^{-6}$ to $0.708266 \pm 38 \times 10^{-6}$ beneath the mT-ES. Rb varies between 0 and 42 ppm with two positive peaks (CT-ES: 33–42 ppm; mT-ES: 1–9 ppm), mirroring the intervals defined by the Sr-isotope ratios; both variations show the exposed surfaces.

Core Ahwaz (AZ)

Sr-isotope ratios of samples derived from core AZ range from $0.707218 \pm 38 \times 10^{-6}$ to $0.708138 \pm 38 \times 10^{-6}$ (Fig. 1; Supplementary data). Two positive $^{87}\text{Sr}/^{86}\text{Sr}$ isotopic peaks at 512 m and 391 m of the core AZ confirm the exact stratigraphic position of the CT-ES (512 m) and mT-ES (391 m) (Fig. 1). In the lithological units below both disconformities, a gradual upward increase in $^{87}\text{Sr}/^{86}\text{Sr}$ ratios is observed, and an abrupt shift to lower $^{87}\text{Sr}/^{86}\text{Sr}$ ratios above the paleo-exposure surfaces. The altered samples beneath the CT-ES indicate the $^{87}\text{Sr}/^{86}\text{Sr}$ ratios between $0.707462 \pm 38 \times 10^{-6}$ and $0.708138 \pm 38 \times 10^{-6}$, while below the mT-ES, range from $0.707812 \pm 30 \times 10^{-6}$ to $0.708006 \pm 36 \times 10^{-6}$. Rb content varies between 0 and 36 ppm with two conspicuous increasing trends (CT-ES: 4–32 ppm; mT-ES: 29–36 ppm), which in their stratigraphic positions match the peaks of the $^{87}\text{Sr}/^{86}\text{Sr}$ ratios.

Core Marun (MN)

In Core MN, $^{87}\text{Sr}/^{86}\text{Sr}$ ratios of the analyzed samples vary between $0.707325 \pm 28 \times 10^{-6}$ and $0.707806 \pm 22 \times 10^{-6}$ (Fig. 1; Supplementary data). Two incremental peaks are observed in the $^{87}\text{Sr}/^{86}\text{Sr}$ ratios at 722 m and 613 m

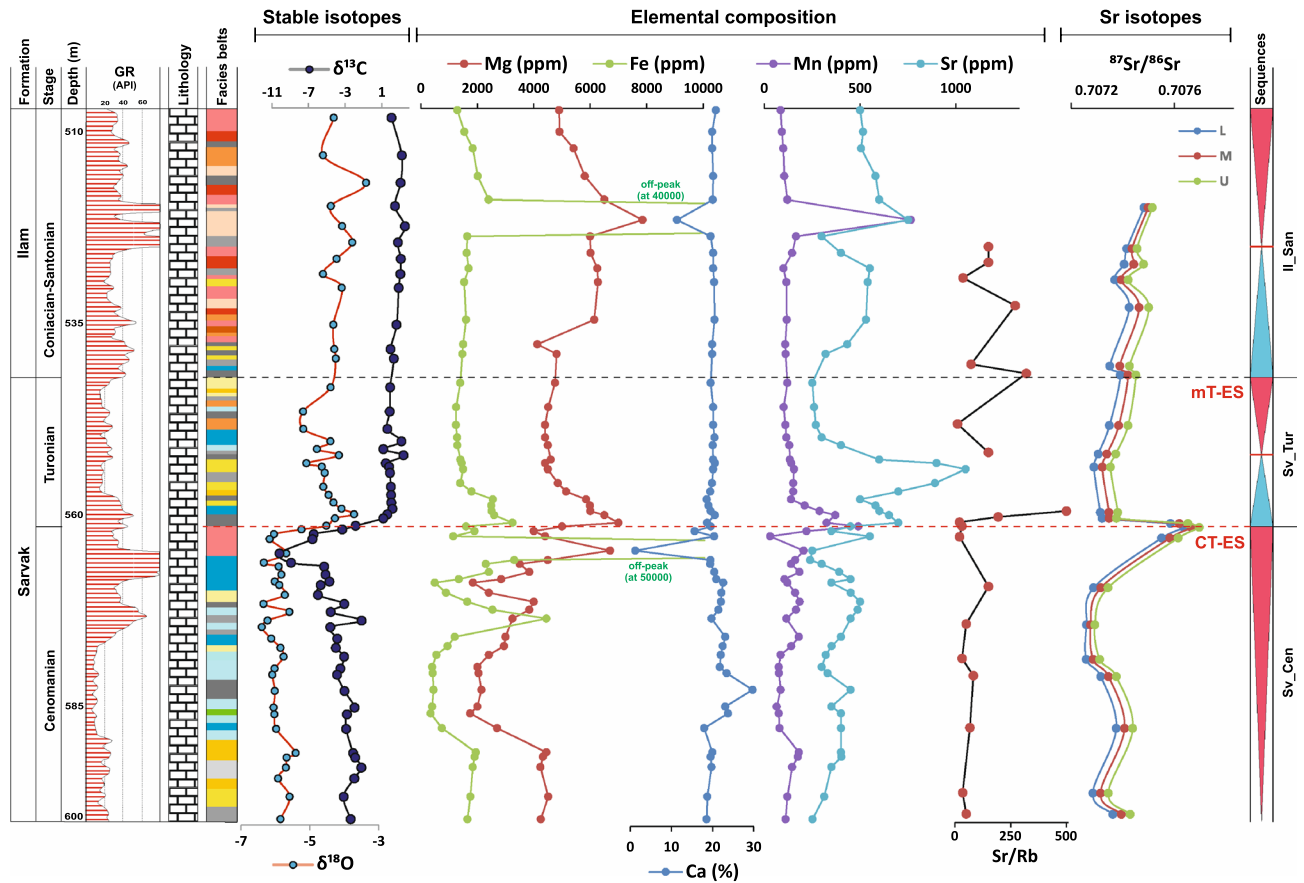


Figure 5. Carbon and oxygen stable isotopes, elemental compositions²³, Rb-corrected $^{87}\text{Sr}/^{86}\text{Sr}$ ratios, and Rb elemental data of the Sarvak and Ilam formations in well GS-2. For lithology and facies pattern, please refer to Fig. 2.

depth, which respectively depict the CT-ES and mT-ES. Stratigraphically, the increase in Rb content also follows these two peaks at 722 and 613 m. Rb minimum and maximum values along the section are 2 ppm and 51 ppm, respectively. Beneath both disconformities, upward increasing trends are observed in $^{87}\text{Sr}/^{86}\text{Sr}$ ratios and Rb contents, with a sudden decrease above the paleo-exposure surfaces.

Core Rag-e Sefid (RS)

The $^{87}\text{Sr}/^{86}\text{Sr}$ ratios from samples of the core RS vary between $0.707268 \pm 30 \times 10^{-6}$ and $0.708126 \pm 26 \times 10^{-6}$, which record two prominent positive peaks around 746–723 m and 661–657 m, showing the CT-ES and mT-ES, respectively. Samples lying immediately below the CT-ES indicate the $^{87}\text{Sr}/^{86}\text{Sr}$ values between $0.707734 \pm 32 \times 10^{-6}$ and $0.708126 \pm 26 \times 10^{-6}$, and beneath the mT-ES show values from 0.707648 ± 22 to 0.707696 ± 38 . In the same intervals, Rb also shows positive peaks (CT-ES: 25–51 ppm; mT-ES: 29–31 ppm). The Rb content varies between 0 and 51 ppm.

Core Gachsaran 1 (GS-1)

In this core, the $^{87}\text{Sr}/^{86}\text{Sr}$ ratios range between $0.707375 \pm 28 \times 10^{-6}$ and $0.707824 \pm 28 \times 10^{-6}$ (Fig. 1). The CT-ES and mT-ES intervals in this core are merged and are expressed through a broad positive peak from 551 to 522 m. The $^{87}\text{Sr}/^{86}\text{Sr}$ ratios of the altered samples vary between $0.707719 \pm 26 \times 10^{-6}$ and $0.707824 \pm 28 \times 10^{-6}$ immediately beneath the merged surface. The Rb content varies between 0 and 41 ppm and shows a positive peak in the same interval. Rb values of the altered samples below the disconformity range from 32 to 41 ppm.

Core Gachsaran 2 (GS-2)

In Core GS-2, the $^{87}\text{Sr}/^{86}\text{Sr}$ ratios vary between the minimum of $0.707321 \pm 32 \times 10^{-6}$ and the maximum of $0.707805 \pm 34 \times 10^{-6}$ (Fig. 1; Supplementary data). CT-ES and mT-ES are characterized by two positive anomalies in $^{87}\text{Sr}/^{86}\text{Sr}$ ratios at stratigraphic positions around 560 m and 545 m depth, respectively. Samples underlying the CT-ES indicate the $^{87}\text{Sr}/^{86}\text{Sr}$ values from $0.707771 \pm 32 \times 10^{-6}$ to $0.707805 \pm 34 \times 10^{-6}$, and underlying the mT-ES show value of $0.707725 \pm 36 \times 10^{-6}$. The Rb content of this core shows a maximum of 29 ppm with two prominent positive peaks. In their stratigraphic position, the Rb peaks follow the positive $^{87}\text{Sr}/^{86}\text{Sr}$ anomalies (CT-ES: 21–29 ppm; mT-ES: 32 ppm). Below both disconformities, a gradual upward increase is observed in the $^{87}\text{Sr}/^{86}\text{Sr}$ ratio and Rb content. Above the paleo-exposure surfaces, they abruptly decrease to significantly lower values.

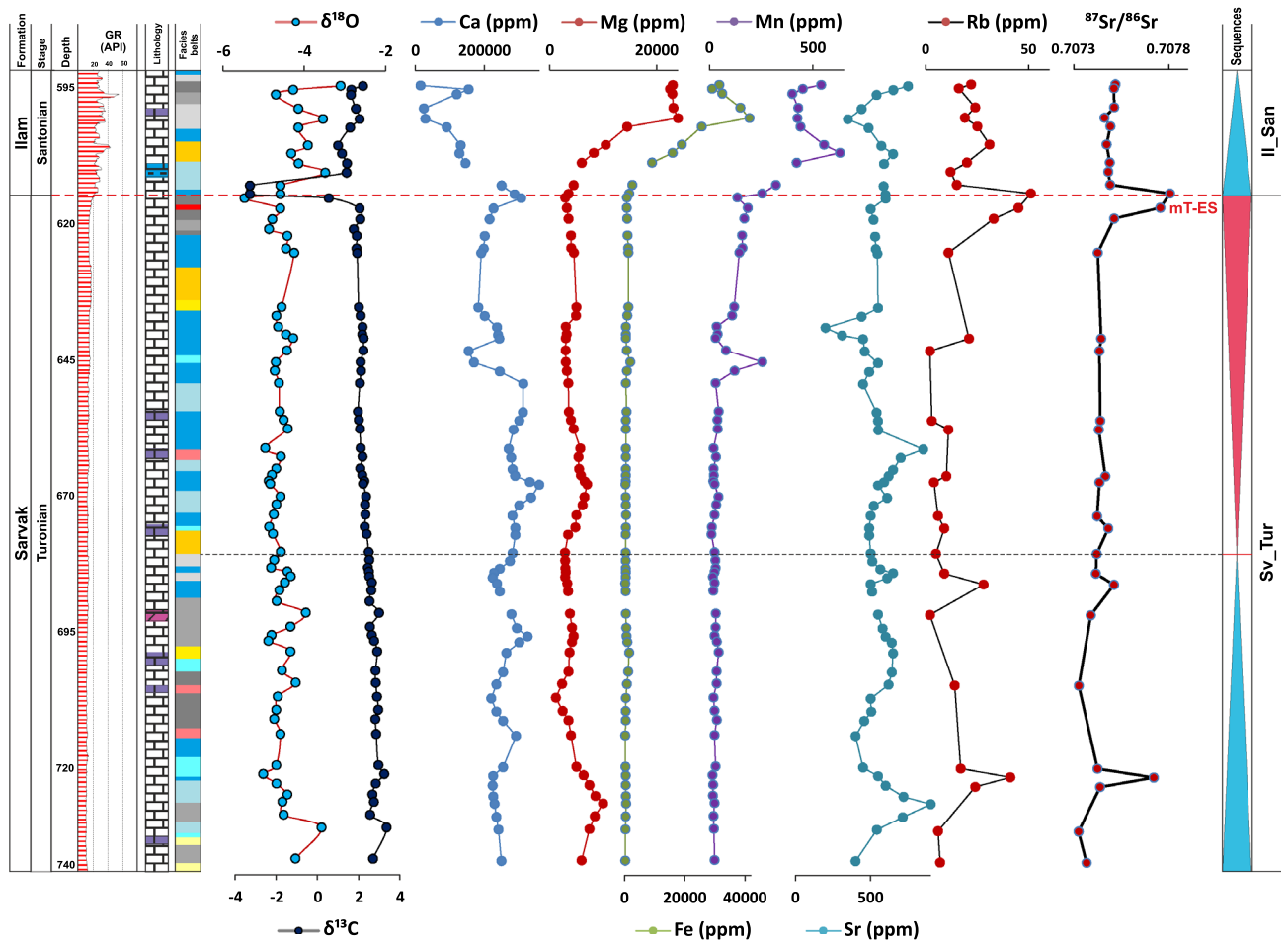


Figure 6. Carbon and oxygen stable isotopes, elemental compositions²³, Rb-corrected $^{87}\text{Sr}/^{86}\text{Sr}$ ratios, and Rb elemental data of the Sarvak and Ilam formations in well MN. Rb elemental data are also from this study. For lithology and facies pattern, please refer to Fig. 2.

Discussion

Disconformity-related $^{87}\text{Sr}/^{86}\text{Sr}$ ratios

The $^{87}\text{Sr}/^{86}\text{Sr}$ ratios of seawater in the Cenomanian-Santonian interval are expected to vary between a minimum of 0.707284 and a maximum of 0.707446 (Look-Up Table Version 4: 08/03)^{50,51}. The $^{87}\text{Sr}/^{86}\text{Sr}$ ratios of the studied intervals mostly fall between these end-members, except for those associated with the disconformities (Fig. 1). The ^{87}Sr and ^{86}Sr isotopes originate from separate sources⁵²; ^{86}Sr is non-radiogenic, but ^{87}Sr is radiogenic and is generated by the radioactive decay of ^{87}Rb . The continental crust has high Rb content because Rb is highly incompatible and tends to be concentrated in magmas during fractional crystallization. Rb^+ can easily substitute for K in K-feldspar, mica, amphibole, and clay minerals, which are abundant in sialic continental crust rocks (*especially upper crust*) and their alteration products. In contrast, mantle rocks and their partial melts are depleted in Rb. These differences led to $^{87}\text{Sr}/^{86}\text{Sr} \sim > 0.708$ for the upper continental crust and < 0.705 for Mid-oceanic Ridge Basalt (MORB-)-like mantle melts⁵³. The $^{87}\text{Sr}/^{86}\text{Sr}$ ratio of seawater and associated marine carbonates over Earth's history has been controlled by the interplay between mantle melts and uptake from the continental crust as a result of the weathering of continental sialic rocks during uplift processes *versus* outpouring of mantle-derived basaltic melts in mid-oceanic ridges and subduction zones⁵⁴. Accordingly, any uptake from riverine sediments originating from the continental upper crust could increase the $^{87}\text{Sr}/^{86}\text{Sr}$ ratio of ocean waters. The increased $^{87}\text{Sr}/^{86}\text{Sr}$ ratio at the CT-ES and mT-ES disconformities, therefore, is assigned to the incorporation of ^{87}Sr from the continental upper crust through higher rates of riverine flux into the shallow marine environment. The most increased continental flux is achieved during orogenesis and probably during active continental magmatism, while the highest mantle flux is achieved during periods of rapid sea-floor spreading⁵³. This suggests that a higher $^{87}\text{Sr}/^{86}\text{Sr}$ ratio at the disconformities could indicate a phase of orogenesis or at least an uplift related to the epeirogeny⁵⁵. More specifically, considering that the $^{87}\text{Sr}/^{86}\text{Sr}$ ratio of the CT-ES and mT-ES falls in the range of the seawater signature (0.706–0.709), the recorded maxima of $^{87}\text{Sr}/^{86}\text{Sr}$ ratios, including 0.708138 in AZ, 0.707806 in MN, and 0.707805 in GS-2 may reflect the uplift of marine limestones⁵⁵. This better supports the weathering of marine limestones rather than the weathering of old continental shields, which could produce much higher $^{87}\text{Sr}/^{86}\text{Sr}$ values. This is consistent with a phase of regional uplift that has been suggested for the Turonian time (mT-ES) throughout the southeastern Neo-Tethyan margin¹⁰.

Based on the long-term $^{87}\text{Sr}/^{86}\text{Sr}$ curves, two negative excursions are expected for the Cretaceous, specifically in the Aptian-Albian and Cenomanian-Santonian time intervals⁵⁶, with the latter simultaneous to the focused time interval of this study. Conversely, our data reveal two remarkably positive excursions throughout Cenomanian-Santonian time. Detailed examinations of the $^{87}\text{Sr}/^{86}\text{Sr}$ isotopic ratios linked to OAE2 indicate a short-term positive excursions in values, particularly during the initial development of OAE2 (the Cenomanian-Turonian boundary), peaking at 0.70747^{46,56}. This brief positive excursion was attributed to climatic changes provoked by OAE2 and associated riverine strontium fluxes⁴⁶. In our study, this time corresponds to the CT-ES; however, $^{87}\text{Sr}/^{86}\text{Sr}$ values vary between 0.70780 (in core AT) and 0.70802 (in core AZ), which are considerably higher. Moreover, for the Turonian stage, a completely plunging trend is observed worldwide, attributed to the breaking marine water stratification and incorporation of large volume of hydrothermal strontium^{46,56}. However, our data indicate another very positive excursion for this time (mT-ES: between 0.70772 in GS-2 and 0.70826 in AT). Since the seawater Sr-isotope curve is considered as a global record of the entire ocean⁵⁷, any variations in the curve necessitate globally impactful alterations in riverine or hydrothermal sources. Therefore, these comparisons dissociate the very positive values in the studied region from global climates and sea-level fluctuations, and they might be explained by regional triggers. Nonetheless, the increase in $^{87}\text{Sr}/^{86}\text{Sr}$ values associated with the CT-ES could be partially, but not entirely, attributed to the global alterations.

A phase of regional uplift has been suggested for the Turonian time (mT-ES) throughout the southeastern Neo-Tethyan margin, which supports the idea of regional rather than the global alteration¹⁰. Diagenetic products beneath the mT-ES, including mature karstification features such as large-scale dissolution, solution-collapsed breccias, and weathered limestone nodules in a clayey matrix (paleosol) further confirm uplift. Similar products are also observed at the CT-ES, indicating a younger karstification stage^{20–23}. However, the role of continental runoff cannot be neglected because, in addition to the $^{87}\text{Sr}/^{86}\text{Sr}$ ratio, the Rb content considerably increases at the disconformities. The increased Rb could explain the elevated $^{87}\text{Sr}/^{86}\text{Sr}$ ratio at these disconformities and their relations to the neighboring continent's uplifting and erosion. However, that assumption is only true if there has been enough time for the ingrowth of ^{87}Sr after deposition, through the ^{87}Rb decay.

Numerical ages of disconformities

To understand the duration of hiatuses associated with disconformities, the Rb-corrected $^{87}\text{Sr}/^{86}\text{Sr}$ of reliable samples bracketing the desired disconformity are converted to the ages according to the Look-Up Table (Version 4: 08/ 03) (Fig. 7)^{50,51}. Their derived numerical ages result in a duration time for the hiatus (Timespan A). However, the selected samples are not directly located beneath and over the disconformity due to the presence

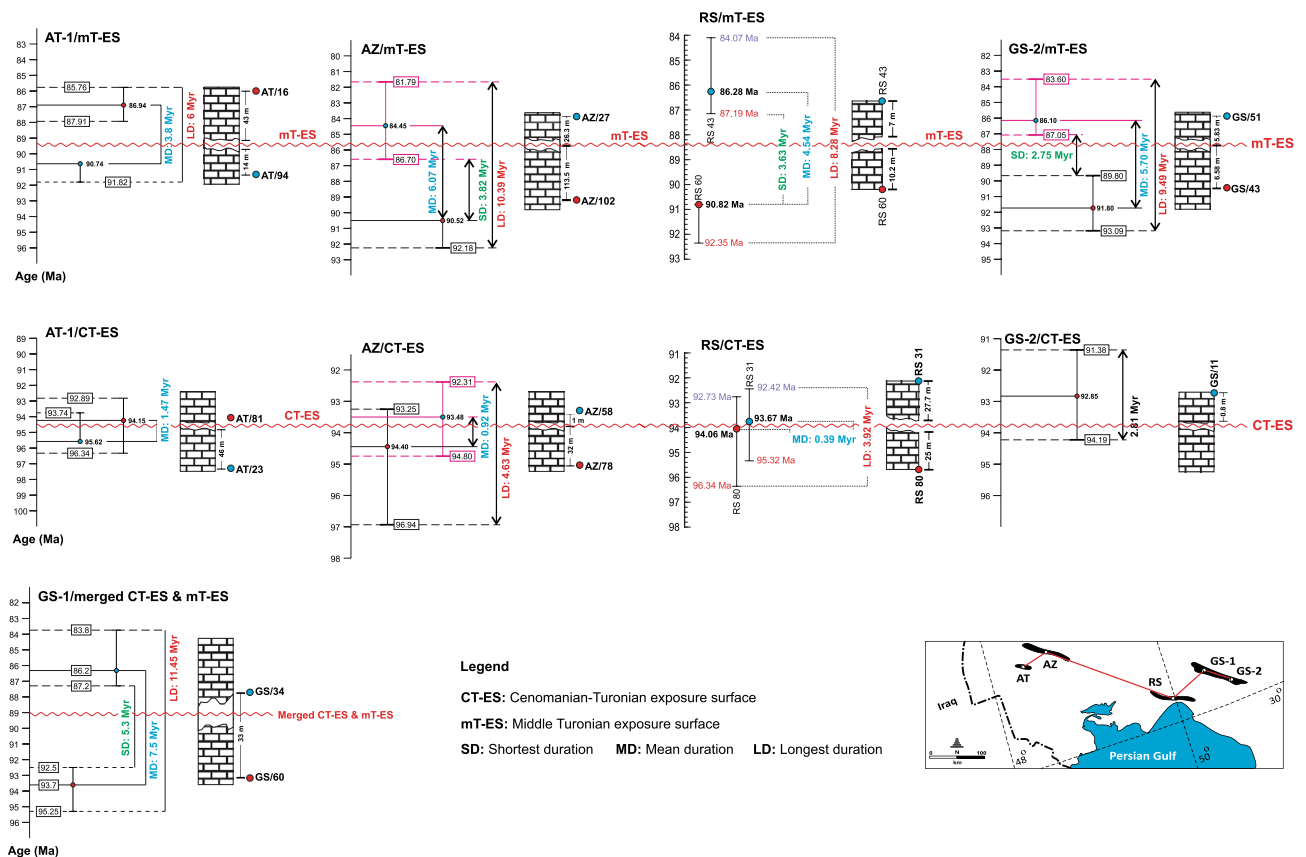


Figure 7. Numerical ages of the samples bracketing the mT-ES and CT-ES disconformities derived from Rb-corrected $^{87}\text{Sr}/^{86}\text{Sr}$ values of the samples. Cores AZ, MN, and GS-2 are from this study. Core RS is from²², cores AN and AT are from²⁰, and Core GS-1 is from²¹.

of a diagenetically altered interval of limestones in between. The altered interval also represents a timespan for deposition which is calculated based on its thickness and the accumulation rates (Timespan B). Therefore, the exact hiatus duration is calculated by subtracting “Timespan B” from “Timespan A”. The commencement of the hiatus is calculated by subtracting the numerical age of the selected sample beneath the disconformity by the calculated deposition timespan of the altered limestones occurring between the sample and the disconformity surface (for detailed methodology refer to²²). Samples confining the CT-ES in Core AZ provide numerical age estimates between 94.4 ± 1.8 and 93.5 ± 1.3 Ma (Fig. 7). In Core GS-2, a sample just above the CT-ES presents an age of 92.9 ± 1.4 Ma. Samples from a sedimentary succession of core AT– enclosing the CT-ES– show age ranges between 95.6 ± 1.9 and 94.2 ± 2.2 Ma²¹, whereas they show ages of 94.0 ± 1.8 and 93.7 ± 1.5 Ma in Core RS²². This means the CT-ES is not older than 95.6 Ma (average: 94.4) and not younger than 92.9 Ma (average: 93.6). Regarding the altered rocks bracketed by the reliable samples (see²² for calculation procedure), the hiatus duration associated with the CT-ES is ~ 0.4 m.yr.

Numerical age estimates for samples from lower and upper parts of the mT-ES are between 90.5 ± 1.7 and 84.5 ± 2.5 Ma in Core AZ and between 91.8 ± 1.6 and 86.1 ± 1.7 Ma in Core GS-2. In addition, samples that surround the mT-ES in Core AT provide age estimates ranging between 90.7 ± 1.1 and 86.9 ± 1.1 Ma²¹ and between 90.8 ± 1.6 and 86.3 ± 1.6 Ma in Core RS²². The oldest age defined for the mT-ES is 91.8 Ma (average: 91.0), whereas the youngest age is 84.5 Ma (average: 86.0). By considering the altered rocks confined by the reliable samples, the hiatus duration of the mT-ES is ~ 4.0 m.yr.

Core GS-1 represents a merged CT-ES and mT-ES. Its lower parts show an age of 93.7 Ma, whereas its upper parts have an age of 86.2 Ma. The lower and upper ages perfectly match the lower age of the CT-ES and upper age of the mT-ES, respectively. Regarding these ages and the altered interval, a hiatus duration of ~ 7.45 m.yr. is calculated for this merged disconformity²¹. Although the Sr-isotope data from Core MN depict the disconformities, we do not include them for calculating numerical ages because they come from core cuttings and are not very robust and reliable.

Correlation with Middle-Late Cretaceous Zagros tectono-magmatic events

Two issues should be considered for understanding the causes of the geochemical disconformities we report in this study. First, what was the cause of the uplift or the sea-level changes during the Late Cretaceous? Second, what were the sources of high Rb and $^{87}\text{Sr}/^{86}\text{Sr}$ uptakes? Although a slight sea-level fall was recorded at about 93.8 Ma around the Cenomanian–Turonian Boundary (CTB)⁵⁸, a regional-scale CT-ES counterpart has not been reported from the central/northwestern Neo-Tethys Ocean. Therefore, the CT-ES disconformity is not solely the product of eustatic sea-level drop. Tectonic inversion has been suggested as the leading cause of the CT-ES in Zagros⁹. The CT-ES and mT-ES disconformities might express the flexural bulging and associated uplift along the Zagros basin of the southeastern Neo-Tethys Ocean. This uplift was also recorded in Turkey and Oman during the Late Cretaceous time and is suggested to be the result of intra-oceanic thrusting and the beginning of oceanic crust emplacement^{59–62}. A late Turonian age (90 Ma) was also proposed for the “obduction” related to the Turonian regional unconformity (mT-ES)^{11,63}.

Subduction initiation and nascent arc formation in the southern Neo-Tethys Ocean have been proposed as responsible for the forearc crust/ophiolite formation during the middle to Late Cretaceous along the Bitlis-Zagros suture zone. These Neo-Tethyan ophiolites have nearly the same age: zircon U–Pb ages of 94–90 Ma for Troodos plagiogranites³⁵; 96–95 Ma for Samail ophiolite gabbros and plagiogranites^{64–67}; 92–91 Ma for Kizildag plagiogranites¹⁸ and 100–96 Ma for Zagros ophiolites⁶⁸ (Fig. 8). The subduction initiation was first generated the forearc oceanic crust and a nascent arc during the subduction of the old Neo-Tethyan oceanic crust beneath the Eurasian plate. The initiation of this subduction triggered the rapid exhumation of the blueschists in Zagros at ~ 70 –86 Ma through the plate rollback^{69,70}. The exhumation of blueschists is also assumed to be associated with higher convergence velocities, plate acceleration, and Oman ophiolite obduction. This also led to oceanic lithospheric buckling¹⁹ in the weak zones during Late Cretaceous, and their timing is consistent with the disconformities we report in this study. Moreover, the age of initial thrusting of the Neo-Tethys Ocean is suggested to occur around 93 Ma⁶² which is close to the cooling age of the metamorphic sole of the Oman ophiolite (94.5 Ma)⁷¹. However, new zircon ages on the Oman metamorphic soles— which could be related to the ophiolite obduction—bracket the timing of prograde garnet and zircon growth in the highest-grade rocks of the metamorphic sole between 96.7 ± 0.1 and 95.2 ± 0.1 Ma and are suggested to overlap with the growth of the overlying ophiolite crust at 96.1 to 95.2 Ma⁷². These ages are similar to the SIS-determined age of the CT-ES, which ranges between 94.4 and 93.6 Ma (Fig. 8). Overall, both disconformities fall in the periods of subduction initiation and exhumation of high-pressure rocks, resulting in compressional forces by tectonic inversion around the CTB in the southeastern Neo-Tethys, which triggered the initial phases of the oceanic closure⁹. This process is assumed to cause a peripheral bulging and associated uplift³⁴. The reason for the two-step (CT-ES and mT-ES) disconformity in the Upper Cretaceous sedimentary strata could be ascribed to the impact of ophiolite formation in two or more localities.

However, although lithosphere buckling, ophiolite obduction, and/or tectonic inversion have been the mechanisms of the uplift and disconformities, the high uptake of Rb and $^{87}\text{Sr}/^{86}\text{Sr}$ is not due to these processes. Oceanic crust generation within the forearcs will produce magmatic rocks with low Rb and less radiogenic $^{87}\text{Sr}/^{86}\text{Sr}$ ratios of ~ 0.702 to 0.703. The new basaltic oceanic crust can gain Sr through interaction with seawater, but it is not a Sr donor. The subduction initiation and plate acceleration due to the increasing convergence velocities between Arabia and Eurasia during the Late Cretaceous could cause the uplift of the Arabian passive margin.

The Arabian Plate is characterized by a thick sequence of Cretaceous siliciclastic sedimentary rocks, which serve as a potential source for the significant influx of Rb and $^{87}\text{Sr}/^{86}\text{Sr}$ into the Neo-Tethys Ocean through uplift and erosion processes. The Dezful Embayment, located in the northwestern segment of the Persian Gulf,

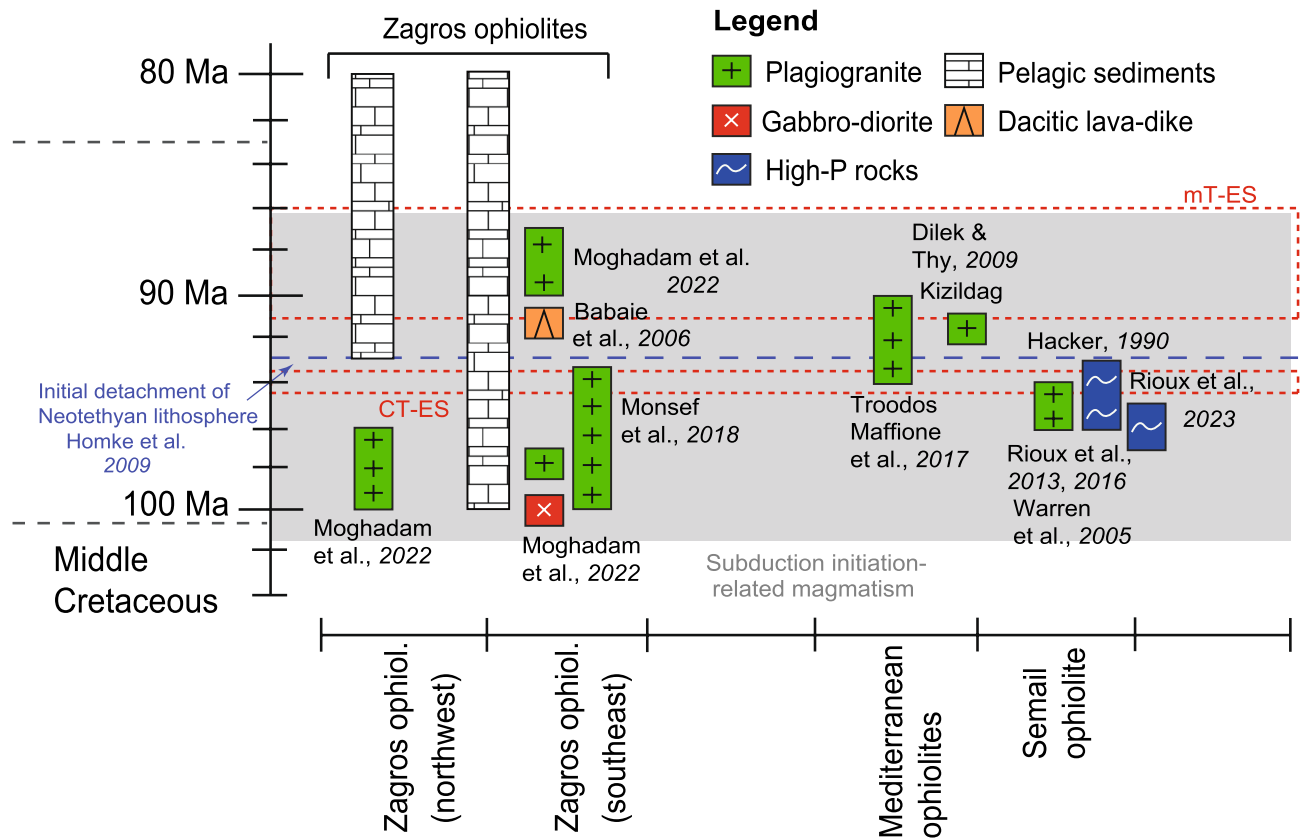


Figure 8. A schematic chart illustrating the chronological sequence of magmatic, high-pressure metamorphic, and sedimentary rocks found in the Zagros, Oman, and Mediterranean ophiolites. Additionally, the chart highlights the occurrences of CT-ES and mT-ES events, along with the initial detachment (intra-oceanic thrusting) of the Neo-Tethyan lithosphere. Please refer to the accompanying text for relevant references.

encompasses several distinct geological units, namely the Gadvan, Kazhdumi, Zubair, and Burgan siliciclastic units. Similar siliciclastic formations, such as the Zubair and Burgan formations, are also present in Saudi Arabia and Kuwait. These siliciclastic rocks likely underwent erosion during the uplift of the Arabian passive margin, concurrent with the deposition of the Sarvak Formation^{30,73,74}.

Paleocurrent observations indicate that during the Cenomanian–Turonian period, the transport direction of siliciclastic sediment fluxes was from the southwest (encompassing the Arabian Plate including Saudi Arabia, Kuwait, and Iraq) towards the northeast (Dezful Embayment). This directional pattern strongly suggests the incorporation of siliciclastic sediments into the Sarvak Formation³⁶.

This study shows that the subduction initiation not only controls the oceanic plate configuration, plate acceleration, or exhumation of the high-pressure rocks but also can cause the nearby continents to be uplifted and eroded. Although radiometric ages of magmatic and metamorphic rocks can provide insights into the timing of forearc formation and subduction initiation-related exhumation, the elemental and Sr isotope analysis of sedimentary sequences offers a more accurate means to determine the age of intra-oceanic thrusting and the construction of oceanic crust in conjunction with nearby continental landmasses.

Ophiolite obduction and intra-oceanic thrusting throughout the southeastern Neo-Tethys are believed to have occurred at different times along a west-to-east trajectory from Troodos (Cyprus), the Mediterranean (Turkey) to Oman, with the latter event occurring later³⁵. Consequently, there is a proposal to analyze the strontium isotope composition of sedimentary sequences containing the studied disconformities across the Middle East in a west-to-east trajectory. This analysis aims to investigate whether the observed temporal pattern is reflected in absolute ages derived from strontium isotope ratios. Such an approach would help determine if strontium isotope analysis of sequences associated with regional disconformities offers a more precise method for defining the age of intra-oceanic thrusting and the formation of oceanic crust.

Data availability

All data generated and/or analyzed in this study are included in this published article and its supplementary information file, and are also available from the corresponding author on reasonable request.

Received: 20 November 2023; Accepted: 8 February 2024

Published online: 12 February 2024

References

- Keller, G., Adatte, T., Berner, Z., Chellai, E. H. & Stueben, D. Oceanic events and biotic effects of the Cenomanian-Turonian anoxic event, Tarfaya Basin, Morocco. *Cretaceous Res.* **29**(5–6), 976–994 (2008).
- Keller, G., Berner, Z., Adatte, T. & Stueben, D. Cenomanian-Turonian and $\delta^{13}\text{C}$, and $\delta^{18}\text{O}$, sea level and salinity variations at Pueblo, Colorado. *Palaeogeogr. Palaeoclimatol. Palaeoecol.* **211**(1–2), 19–43 (2004).
- Larson, R. L. Geological consequences of superplumes. *Geology* **19**(10), 963–966 (1991).
- Leckie, R. M., Bralower, T. J. & Cashman, R. Oceanic anoxic events and plankton evolution: Biotic response to tectonic forcing during the mid-Cretaceous. *Paleoceanography* **17**(3), 13–21 (2002).
- Piryaei, A., Reijmer, J. J. G., Borgomano, J. & van Buchem, F. S. P. Late Cretaceous tectonic and sedimentary evolution of the Bandar Abbas Area, Fars Region, Southern Iran. *J. Petrol. Geol.* **34**(2), 157–180 (2011).
- Piryaei, A. *et al.* The influence of Late Cretaceous tectonic processes on sedimentation patterns along the northeastern Arabian plate margin (Fars Province, SW Iran). In *Geological Society Special Publication*. 211–251 (2010).
- Moghadam, H. S. & Stern, R. J. Subduction initiation causes broad upper plate extension: The late Cretaceous Iran example. *Lithos* **398**, 106296 (2021).
- Moghadam, H. S. *et al.* Subduction initiation and back-arc opening north of Neo-Tethys: Evidence from the late Cretaceous Torbat-e-Heydarieh ophiolite of NE Iran. *GSA Bull.* **132**(5–6), 1083–1105 (2020).
- Navidtalab, A., Sarfi, M., Enayati-Bidgoli, A. & Yazdi-Moghadam, M. Syn-depositional continental rifting of the Southeastern Neo-Tethys margin during the Albian–Cenomanian: evidence from stratigraphic correlation. *Int. Geol. Rev.* **62**(13–14), 1698–1723 (2020).
- Berberian, M. & King, G. C. P. Towards a paleogeography and tectonic evolution of Iran. *Canadian J. Earth Sci.* **18**(2), 210–265 (1981).
- Alavi, M. Structures of the Zagros fold-thrust belt in Iran. *Am. J. Sci.* **307**(9), 1064–1095 (2007).
- Ahmadhadi, F., Lacombe, O. & Daniel, J.-M. Early Reactivation of Basement Faults in Central Zagros (SW Iran): Evidence from Pre-folding Fracture Populations in Asmari Formation and Lower Tertiary Paleogeography. In *Thrust Belts and Foreland Basins* (eds Lacombe, O. *et al.*) 205–228 (Springer, 2007).
- Bagherpour, B., Mehrabi, H., Faghih, A., Vaziri-Moghaddam, H. & Omidvar, M. Tectono-eustatic controls on depositional setting and spatial facies distribution of Coniacian-Santonian sequences of the Zagros Basin in Fars area S. Iran. *Marine Petrol. Geol.* **129**, 105072 (2021).
- Mehrabi, H., Bagherpour, B., & Honarmand, J. Reservoir quality and micrite textures of microporous intervals in the Upper Cretaceous successions in the Zagros area, SW Iran. *J. Petrol. Sci. Eng.* 107292 (2020).
- Mehrabi, H. & Rahimpour-Bonab, H. Paleoclimate and tectonic controls on the depositional and diagenetic history of the Cenomanian-early Turonian carbonate reservoirs, Dezful Embayment SW Iran. *Facies* **60**(1), 147–167 (2014).
- Mehrabi, H., Rahimpour-Bonab, H., Hajikazemi, E. & Jamalian, A. Controls on depositional facies in Upper Cretaceous carbonate reservoirs in the Zagros area and the Persian Gulf Iran. *Facies* **61**(4), 23 (2015).
- Wennberg, O. *et al.* The Khaviz Anticline: An outcrop analogue to giant fractured Asmari Formation reservoirs in SW Iran. *Geol. Soc. London Special Publ.* **270**(1), 23–42 (2007).
- Dilek, Y. & Thy, P. Island arc tholeiite to boninitic melt evolution of the Cretaceous Kizildag (Turkey) ophiolite: Model for multi-stage early arc-forearc magmatism in Tethyan subduction factories. *Lithos* **113**(1–2), 68–87 (2009).
- Agard, P., Jolivet, L., Vrielynck, B., Burov, E. & Monie, P. Plate acceleration: The obduction trigger?. *Earth Planet. Sci. Lett.* **258**(3–4), 428–441 (2007).
- Mehrabi, H., Navidtalab, A., Enayati, A. & Bagherpour, B. Age, duration, and geochemical signatures of paleo-exposure events in Cenomanian-Santonian sequences (Sarvak and Ilam formations) in SW Iran: Insights from carbon and strontium isotopes chemostratigraphy. *Sediment. Geol.* **434**, 106136 (2022).
- Mehrabi, H., Navidtalab, A., Rahimpour-Bonab, H. & Heimhofer, U. Geochemical expression of sequence stratigraphic surfaces: A case from Upper Cretaceous shallow-water carbonates of southeastern Neo-Tethys margin. *SW Iran. Cretaceous Res.* **140**, 105329 (2022).
- Navidtalab, A., Rahimpour-Bonab, H., Huck, S. & Heimhofer, U. Elemental geochemistry and strontium-isotope stratigraphy of Cenomanian to Santonian neritic carbonates in the Zagros Basin Iran. *Sediment. Geol.* **346**, 35–48 (2016).
- Rahimpour-Bonab, H. *et al.* Palaeo-exposure surfaces in Cenomanian–Santonian carbonate reservoirs in the dezful embayment, SW Iran. *J. Petrol. Geol.* **36**(4), 335–362 (2013).
- Rahimpour-Bonab, H., Mehrabi, H., Enayati-Bidgoli, A. H. & Omidvar, M. Coupled imprints of tropical climate and recurring emergence on reservoir evolution of a mid Cretaceous carbonate ramp, Zagros Basin, southwest Iran. *Cretaceous Res.* **37**, 15–34 (2012).
- Vincent, B. *et al.* Depositional sequences, diagenesis and structural control of the Albian to Turonian carbonate platform systems in coastal Fars (SW Iran). *Marine Petrol. Geol.* **63**, 46–67 (2015).
- van Buchem, F. S. *et al.* High resolution sequence stratigraphy of the Natih Formation (Cenomanian/Turonian) in northern Oman: Distribution of source rocks and reservoir facies. *GeoArabia* **1**(1), 65–91 (1996).
- Al-Husseini, M. I. Late albian, cenomanian and turonian natih supersequence of Oman: Type section for Orbiton 7 (103.6–89.0 Ma). *GeoArabia*, **15**(4): 125–142 (2010).
- Hollis, C. & Sharp, I. Albian-cenomanian-turonian carbonate-siliciclastic systems of the Arabian plate: Advances in diagenesis, structure and reservoir modelling—introduction. *Petrol. Geosci.* **17**(3), 207–209 (2011).
- Nairn, A. & Alsharhan, A. Sedimentary basins and petroleum geology of the Middle East. Elsevier (1997).
- Bromhead, A., van Buchem, F., Simmons, M. & Davies, R. Sequence stratigraphy, palaeogeography and petroleum plays of the cenomanian-turonian succession of the Arabian plate: AN updated synthesis. *J. Petrol. Geol.* **45**(2), 119–161 (2022).
- Chen, P., Guo, L., Li, C. & Tong, Y. Karstification characteristics of the Cenomanian-Turonian Mishrif Formation in the Missan Oil Fields, southeastern Iraq, and their effects on reservoirs. *Front. Earth Sci.* **16**(2), 435–445 (2022).
- Mahdi, T. & Aqrabi, A. Sequence stratigraphic analysis of the mid-Cretaceous Mishrif formation, southern Mesopotamian basin Iraq. *J. Petrol. Geol.* **37**(3), 287–312 (2014).
- Mulayim, O., Yilmaz, O., Sari, B., Tasli, K. & Wagreich, M. Cenomanian-Turonian drowning of the Arabian Carbonate Platform, the İnşidere section, Adiyaman, SE Turkey. *Geol. Soc. London Special Publ.* **498**(1), 189–210 (2020).
- Hollis, C. Diagenetic controls on reservoir properties of carbonate successions within the Albian-Turonian of the Arabian Plate. *Petrol. Geosci.* **17**(3), 223–241 (2011).
- Maffione, M., van Hinsbergen, D. J., de Gelder, G. I., van der Goes, F. C. & Morris, A. Kinematics of late Cretaceous subduction initiation in the Neo-Tethys Ocean reconstructed from ophiolites of Turkey, Cyprus, and Syria. *J. Geophys. Res. Solid Earth* **122**(5), 3953–3976 (2017).
- Barrier, É., Vrielynck, B., & Brunet-Lourdin M. F. Paleotectonic reconstruction of the central Tethyan Realm: Tectono-Sedimentary-Palinspastic Maps from Late Permian to Pliocene: Atlas of 20 Maps. (2018).
- Hajikazemi, E., Al-Aasm, I. & Coniglio, M. Subaerial exposure and meteoric diagenesis of the Cenomanian-Turonian Upper Sarvak Formation, southwestern Iran. *Geol. Soc. London Special Publications* **330**(1), 253–272 (2010).

38. Hajikazemi, E., Al-Aasm, I. S. & Coniglio, M. Chemostratigraphy of cenomanian-turonian carbonates of the sarvak formation, Southern Iran. *J. Petrol. Geol.* **35**(2), 187–205 (2012).
39. McArthur, J. M. & Howarth, R. J. Sr-isotope stratigraphy. *Geol. Timescale* **2004**, 96–105 (2004).
40. Faure, G., & Mensing, T.M. *Isotopes: principles and applications*. Wiley, (2004).
41. McArthur, J. M. Recent trends in strontium isotope stratigraphy. *Terra Nova* **6**(4), 331–358 (1994).
42. Allan, J. R. & Wiggins, W. D. Dolomite reservoirs: Geochemical techniques for evaluating origin and distribution. *AAPG Short Course Note Ser.* **36**, 170 (1993).
43. Ogg, J.G., Ogg, G., & Gradstein, F.M. *A concise geologic time scale: 2016*. Elsevier, (2016).
44. Veizer, J. *et al.* 87Sr/86Sr, $\delta^{13}\text{C}$ and $\delta^{18}\text{O}$ evolution of Phanerozoic seawater. *Chem. Geol.* **161**(1), 59–88 (1999).
45. Brand, U. & Veizer, J. Chemical diagenesis of a multicomponent carbonate system-1. Trace elements. *J. Sediment. Petrol.* **50**(4), 1219–1236 (1980).
46. Frijia, G. & Parente, M. Strontium isotope stratigraphy in the upper Cenomanian shallow-water carbonates of the southern Apennines: Short-term perturbations of marine 87 Sr/86 Sr during the oceanic anoxic event 2. *Palaeogeography Palaeoclimatol. Palaeoecol.* **261**(1), 15–29 (2008).
47. Steuber, T., Korbar, T., Jelaska, V. & Gušić, I. Strontium-isotope stratigraphy of upper Cretaceous platform carbonates of the island of Brač (Adriatic Sea, Croatia): Implications for global correlation of platform evolution and biostratigraphy. *Cretaceous Res.* **26**(5), 741–756 (2005).
48. McArthur, J. M., Howarth, R. J., & Shields, G.A. Strontium Isotope Stratigraphy. In *The Geologic Time Scale 2012*. p. 127–144. (2012).
49. Gradstein, F.M., Ogg, J.G., Schmitz, M.D., & Ogg, G.M. *Geologic Time Scale 2020*. Elsevier (2020).
50. Howarth, R. J. & McArthur, J. M. Statistics for strontium isotope stratigraphy: A robust LOWESS fit to the marine Sr-isotope curve for 0 to 206 Ma, with look-up table for derivation of numeric age. *J. Geol.* **105**(4), 441–456 (1997).
51. McArthur, J. M., Howarth, R. J. & Bailey, T. R. Strontium isotope stratigraphy: LOWESS version 3: Best fit to the marine Sr-isotope curve for 0–509 Ma and accompanying look-up table for deriving numerical age. *J. Geol.* **109**(2), 155–170 (2001).
52. Faure, G., Powell, J. L. *Strontium isotope geology*. Vol. 5. Springer Science & Business Media. (1972).
53. Veizer, J. Strontium isotopes in seawater through time. *Annual Rev. Earth Planet. Sci.* **17**, 141 (1989).
54. Brass, G. W. The variation of the marine 87Sr/86Sr ratio during Phanerozoic time: interpretation using a flux model. *Geochimica et Cosmochimica Acta* **40**(7), 721–730 (1976).
55. Elderfield, H. Strontium isotope stratigraphy. *Palaeogeography Palaeoclimatol. Palaeoecol.* **57**(1), 71–90 (1986).
56. Jones, C. E. & Jenkyns, H. C. Seawater strontium isotopes, oceanic anoxic events, and seafloor hydrothermal activity in the Jurassic and Cretaceous. *Am. J. Sci.* **301**(2), 112–149 (2001).
57. Capo, R. & DePaolo, D. Homogeneity of Sr isotopes in the oceans. *EOS Trans. Am. Geophys. Union* **73**, 272 (1992).
58. Haq, B. U. Cretaceous eustasy revisited. *Global Planet. Change* **113**, 44–58 (2014).
59. Robertson, A. & Searle, M. The northern Oman Tethyan continental margin: stratigraphy, structure, concepts and controversies. *Geol. Soc. London Special Publ.* **49**(1), 3–25 (1990).
60. Stoneley, R. The Arabian continental margin in Iran during the late Cretaceous. *Geol. Soc. London Special Publ.* **49**(1), 787–795 (1990).
61. Farzadi, P. The development of middle Cretaceous carbonate platforms, Persian Gulf, Iran: Constraints from seismic stratigraphy, well and biostratigraphy. *Petrol. Geosci.* **12**(1), 59–68 (2006).
62. Homke, S. *et al.* Late Cretaceous-paleocene formation of the proto-Zagros foreland basin, Lurestan Province, SW Iran. *Bull. Geol. Soc. Am.* **121**(7–8), 963–978 (2009).
63. Alavi, M. Regional stratigraphy of the Zagros fold-thrust belt of Iran and its proforeland evolution. *Am. J. Sci.* **304**(1), 1–20 (2004).
64. Warren, C. J., Parrish, R. R., Waters, D. J. & Searle, M. P. Dating the geologic history of Oman's Semail ophiolite: Insights from U-Pb geochronology. *Contrib. Mineral. Petrol.* **150**(4), 403–422 (2005).
65. Rioux, M. *et al.* Synchronous formation of the metamorphic sole and igneous crust of the Semail ophiolite: New constraints on the tectonic evolution during ophiolite formation from high-precision U-Pb zircon geochronology. *Earth Planet. Sci. Lett.* **451**, 185–195 (2016).
66. Rioux, M. *et al.* Rapid crustal accretion and magma assimilation in the Oman-UAE ophiolite: High precision U-Pb zircon geochronology of the gabbroic crust. *J. Geophys. Res. Solid Earth.* **117** (2012).
67. Rioux, M. *et al.* Tectonic development of the Semail ophiolite: High-precision U-Pb zircon geochronology and Sm-Nd isotopic constraints on crustal growth and emplacement. *J. Geophys. Res. Solid Earth* **118**(5), 2085–2101 (2013).
68. Moghadam, H. S. *et al.* The middle-late Cretaceous Zagros ophiolites, Iran: Linking of a 3000 km swath of subduction initiation fore-arc lithosphere from Troodos, Cyprus to Oman. *Bulletin* **134**(5–6), 1414–1442 (2022).
69. Moghadam, H. S. *et al.* Subduction, high-P metamorphism, and collision fingerprints in South Iran: Constraints from zircon U-Pb and mica Rb-Sr geochronology. *Geochem. Geophys. Geosyst.* **18**(1), 306–332 (2017).
70. Angiboust, S., Agard, P., Glodny, J., Omrani, J. & Oncken, O. Zagros blueschists: Episodic underplating and long-lived cooling of a subduction zone. *Earth Planetary Sci. Lett.* **443**, 48–58 (2016).
71. Warren, C. J., Parrish, R. R., Waters, D. J. & Searle, M. P. Dating the geologic history of Oman's Semail ophiolite: Insights from U-Pb geochronology. *Contrib. Mineral. Petrol.* **150**(4), 403–422 (2005).
72. Rioux, M., *et al.* The temporal evolution of subduction initiation in the Semail ophiolite: High-precision U-Pb zircon petrochronology of the metamorphic sole. *J. Metamorph. Geol.* (2023).
73. Alsharhan, A.S. Petroleum systems in the Middle East. In *Geological Society Special Publication*. 361–408. (2014).
74. Sharland, P. R. *et al.* Arabian plate sequence stratigraphy. *GeoArabia* **2**, 1–371 (2001).
75. Omidvar, M. *et al.* Revision of the foraminiferal biozonation scheme in Upper Cretaceous carbonates of the Dezful Embayment, Zagros, Iran: Integrated palaeontological, sedimentological and geochemical investigation. *Revue de Micropaleontologie* **57**(3), 97–116 (2014).

Acknowledgements

All logistical support for this study came from Damghan University and the University of Tehran, Iran. We appreciate the National Iranian Oil Company for analytical support.

Author contributions

A.N. and H.R. conceived and designed the project with input from H.M. and A.N. collected the rock samples used in this study. H.M. analyzed the thin-sections and well-logs, prepared sedimentological logs, with input from H.R. established the stratigraphy, A.N. carried out the micro-sampling for geochemical analyses and stable isotope measurements. H.S. carried out the re-evaluation of the published magmatic data. A.N. and H.S. wrote the manuscript with input from all authors.

Competing interests

The authors declare no competing interests.

Additional information

Supplementary Information The online version contains supplementary material available at <https://doi.org/10.1038/s41598-024-54128-3>.

Correspondence and requests for materials should be addressed to A.N.

Reprints and permissions information is available at www.nature.com/reprints.

Publisher's note Springer Nature remains neutral with regard to jurisdictional claims in published maps and institutional affiliations.



Open Access This article is licensed under a Creative Commons Attribution 4.0 International License, which permits use, sharing, adaptation, distribution and reproduction in any medium or format, as long as you give appropriate credit to the original author(s) and the source, provide a link to the Creative Commons licence, and indicate if changes were made. The images or other third party material in this article are included in the article's Creative Commons licence, unless indicated otherwise in a credit line to the material. If material is not included in the article's Creative Commons licence and your intended use is not permitted by statutory regulation or exceeds the permitted use, you will need to obtain permission directly from the copyright holder. To view a copy of this licence, visit <http://creativecommons.org/licenses/by/4.0/>.

© The Author(s) 2024